Computational Study of Vortex-Induced Separation for a 5-Bladed Rotor

Christopher S. Thurman
Research Aerospace Engineer
NASA Langley Research Center
Hampton, VA, USA

Nikolas S. Zawodny
Senior Research Aerospace Engineer
NASA Langley Research Center
Hampton, VA, USA

Kyle A. Pascioni
Research Aerospace Engineer
NASA Langley Research Center
Hampton, VA, USA

ABSTRACT

This work computationally investigated the rotor blade vortex-induced separation recently observed during an aerodynamic rotor test campaign in the NASA Langley Research Center 14- by 22-Foot Subsonic Tunnel. Two separate approaches (i.e., airfoil modification and blade tip modification) were studied to mitigate the vortex-induced separation. Mid-fidelity tools based on blade element momentum theory were shown to mispredict the rotor inflow and were also shown to not capture the vortex-induced separation caused by perpendicular blade-vortex interaction. This misprediction was exploited to isolate the aerodynamic thrust deficit caused by the vortex-induced separation (20%) from the thrust deficit due to inflow variation (31%). High-fidelity tools were shown to reasonably predict aerodynamic forces within 13% and flow separation when compared to experimental results. The modified airfoil variant of the baseline rotor effectively mitigated the vortex-induced separation, while the blade tip modified variant still showed separation, though the size and strength of the vortex was reduced. Acoustic predictions were underpredicted by 10 dB from preliminary measurements taken in the untreated wind tunnel. Broadband noise contributions from different rotor blade sections showed that self-noise due to flow separation and other turbulent boundary layer mechanisms was the dominant noise source for all three rotor cases, followed by blade-wake interaction noise caused by perpendicular blade-vortex interactions.

NOMENCLATURE

$c(r)$	Rotor chord length distribution, in
C_Q	Torque coefficient, $\frac{Q}{\rho A(\Omega R)^3}$
c_r	Chord length at the r spanwise location, in
c_{tip}	Chord length at the rotor tip, in
C_T	Thrust coefficient, $\frac{T}{\rho A(\Omega R)^2}$
M_{tip}	Mach number at the rotor blade tip
M_∞	Freestream Mach number
N_b	Number of rotor blades
p_{ref}	Reference pressure, 20 μPa
P_{xx}	Power spectral density, Pa^2/Hz
Q	Rotor generated torque, ft-lb
r	Normalized span location, $\frac{x}{R}$
R	Rotor radius, in
Re_c	Chord-based Reynolds number
SPL	Sound pressure level, dB
$\text{SPL}_{1/3}$	One-third octave sound pressure level, dB
T	Rotor generated thrust, lb
TKE	Turbulent kinetic energy, ft^2/s^2
V_{mag}	Velocity magnitude, ft/s
V_z	Vertical component of velocity, ft/s
x_c	Nondimensional chord length
y	Radial observer location relative to center of rotor rotation, ft
y^+	Normalized wall distance
α	Angle of attack, deg
α_0	Airfoil zero lift angle of attack, rad
Δf	Narrowband spectra frequency resolution, Hz
Δs	Finest voxel size, in
Θ_{obs}	Observer angle relative to rotor plane, deg
$\theta_{tw}(r)$	Rotor twist distribution, rad
κ_h	Empirical inflow correction factor for hover
ρ	Fluid density, slugs/in^3
$\sigma(r)$	Rotor solidity distribution, $\frac{N_b c(r)}{\pi R}$
Ω	Rotor rotational rate, revolutions per minute (RPM)

Presented at the Vertical Flight Society's 79th Annual Forum & Technology Display, Palm Bay, FL, May 16–18, 2023.

INTRODUCTION

The past decade has seen considerable interest in Advanced Air Mobility (AAM) vehicles, capable of transporting personnel and packages across various environments in a safe and sustainable way. These vehicles are typically comprised of multirotor systems and generally range in size from small unmanned aerial systems (sUAS), i.e., drones, to single- or multipassenger vehicles designed for operation in urban environments. The rotor systems on AAM vehicles can often be unconventional and may incorporate collective pitch, rotor speed, rotor shaft tilt angle, or combinations of these controls to support operational conditions ranging from vertical takeoff/landing (VTOL), through transitional modes, to 'cruise,' or forward flight with the rotor(s) orthogonal to the oncoming flow.

Though the AAM industry is growing at a rapid pace, noise is still a large inhibitor toward the development and real-world application of these AAM vehicles, which has motivated research in identifying and characterizing noise sources produced by rotor systems in various operational conditions. To this end, a two-part experimental campaign in the NASA Langley Research Center 14- by 22-Foot Subsonic Tunnel has been planned to explore the aerodynamic and acoustic behavior of representative AAM rotors operating in hover, transition, and cruise conditions. The first part of this campaign dealt primarily with aerodynamic characterization and is the subject of a companion paper (Ref. 1). During the first part of this campaign, one of the two tested rotor geometries encountered separation caused by blade impingement of the tip vortex from a preceding blade (i.e., perpendicular blade-vortex interaction (BVI)) in the hover operating condition. These perpendicular BVIs are known to cause broadband blade-wake interaction (BWI) noise emanating from the blade leading edge. Though BWI noise caused by perpendicular BVI has been studied extensively for stationary airfoils (Refs. 2–4) and for rotors in edgewise forward flight (Refs. 5–8), limited work has been done toward its characterization for hovering rotors (Refs. 9, 10). Moreover, these studies were aimed at understanding the tip vortex physics and subsequent BWI noise rather than aerodynamic changes about the blade undergoing perpendicular BVI, which has been scarcely studied (Ref. 11).

The purpose of this work will be to aerodynamically and acoustically investigate the blade boundary layer separation caused by perpendicular BVI observed on a 5-bladed rotor tested in the NASA Langley Research Center 14- by 22-Foot Subsonic Tunnel (Ref. 1) using mid- and high-fidelity computational tools. Two blade design modifications will also be explored to mitigate the effect of vortex-induced separation.

TECHNICAL APPROACH

Rotor Design

The baseline rotor geometry used throughout this work was the optimum 5-bladed rotor used in a companion paper (Ref. 1) and shown in Fig. 1, hereby denoted as the OPT5 rotor. Though two rotor geometries were used in Ref. 1, only the OPT5 required additional high-fidelity computations to identify complex problematic aerodynamic phenomena detailed herein.

An ‘optimum hovering rotor’ can be defined as one that has both minimal induced power requirements and minimal profile power requirements (Ref. 12) using blade element momentum theory (BEMT). The minimal induced power comes from a twist distribution,

$$\theta_{tw}(r) = \frac{1}{r}\left(\frac{4C_{T_{\text{design}}}}{5.73\sigma(r)} + \sqrt{\frac{C_{T_{\text{design}}}}{2}}\right) - \alpha_0, \qquad (1)$$

which is designed to produce uniform inflow over the blade span. The minimal profile power comes from a tapered chord distribution,

$$c(r) = \frac{c_{\text{tip}}}{r}, \qquad (2)$$

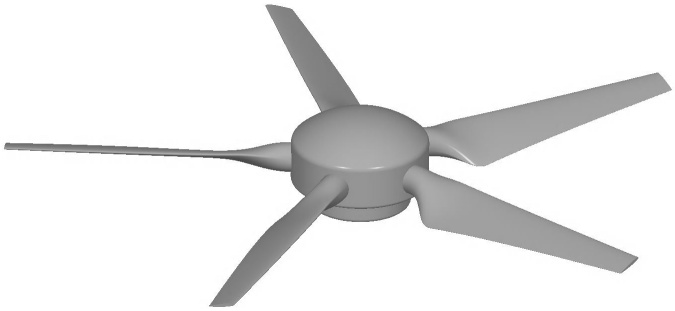

Figure 1: Simplified OPT5 rotor geometry.

which allows for each radial station to operate at an optimal lift-to-drag ratio. In these equations, r is the normalized span location, $C_{T_{\text{design}}}$ is the desired thrust coefficient, $\sigma(r)$ is the spanwise distribution of solidity, α_0 is the zero lift angle of attack of the airfoil, and c_{tip} is the chord length at the blade tip. A taper distribution of this form is typically not physically realizable, so a linear taper distribution is used in practice.

A 2-bladed variant of the ‘optimum hovering rotor’ was evaluated in Refs. 13–15 during anechoic chamber and wind tunnel testing campaigns, and an OPT5 rotor was also designed with an NACA 0012 airfoil for use on a tiltwing vehicle platform in Ref. 16. Since the focus of the wind tunnel testing campaign detailed in Ref. 1 was rotor transition regimes, the OPT5 rotor of Ref. 16 was selected as one of the rotor designs used for that work. However, the OPT5 was scaled down to model size by a factor of 3.61 while maintaining typical nondimensional rotor quantities such as $C_T/\sigma_{mean} = 0.123$, a disk loading of $\text{DL} = 20$ lb/ft^2, and a tip Mach number of $M_{\text{tip}} = 0.50$ in the hover operating condition. The scaled-down geometry had a disk radius of $R = 12$ in, $c_{\text{tip}} = 0.97$ in, and was designed to produce $T_{\text{design}} = 62.85$ lb of thrust at a target rotor speed of $\Omega = 5332$ RPM. The resultant twist and taper distributions produced using Eqs. 1 and 2, as well as the linear taper distribution that was used for the OPT5 rotor are shown in Fig. 2.

As will be discussed in subsequent sections, the measured aerodynamic performance differences of the OPT5 from the design condition observed in Ref. 1 were thought to be caused by perpendicular blade-vortex interaction (BVI). Because of this, two variants of the OPT5 were computationally studied to investigate methods for reducing the aerodynamic effect of perpendicular BVI.

The first of these variants entailed changing the airfoil profile of the OPT5 to an NACA 63A-612 and will hereby be denoted as the OPT5 modified airfoil rotor (OPT5-MA). This 6-series NACA airfoil was selected over other typically used rotorcraft airfoils (e.g., Boeing-Vertol VR series, Sikorsky SC series) primarily for its superior stall characteristics at low Reynolds numbers like those typically associated with AAM vehicles. It was shown in Ref. 10 that increasing C_T could increase the vertical separation distance between a preceding tip vortex and the leading edge of a rotor blade, leading to a decrease in BWI noise, so the $0.06c$ camber associated with the NACA

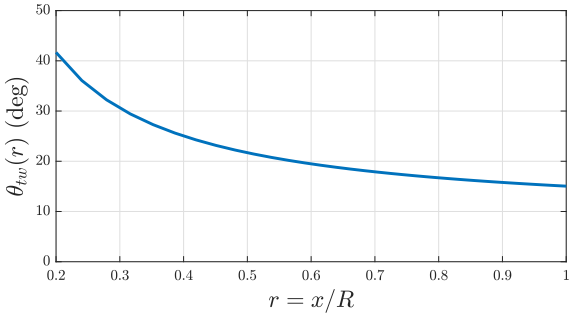

(a) Spanwise twist distribution.

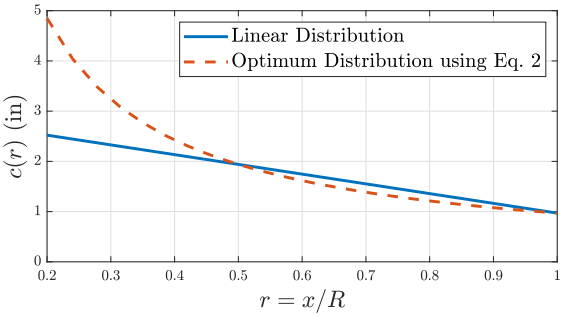

(b) Spanwise chord distribution.

Figure 2: OPT5 rotor blade characteristics.

63A-612 airfoil was thought to aid in this regard. The Comprehensive Analytical Model of Rotorcraft Aerodynamics and Dynamics (CAMRAD II) (Ref. 17) was used to determine Ω for the OPT5-MA such that it produced the same T_{design} as the OPT5. The resulting rotor speed was found to be $\Omega = 4355$ RPM.

The second variant modified the OPT5 blade to include 20° of anhedral and 20° of backward sweep beginning at the $0.95R$ spanwise location. The anhedral/sweep was thought to increase the vertical separation distance between a preceding tip vortex and the leading edge of a rotor blade since the tip vortex formation would occur slightly below the rotor plane. In addition to these modifications, extra taper was added between the $0.95R$ spanwise location and the blade tip, such that $c_{\text{tip}} = 0.485$ in. This additional taper over the OPT5 blades was added to decrease the size and strength of the tip vortex. This second variant will be referred to as the OPT5 modified blade rotor (OPT5-MB), and an illustration of the blade modification near the tip is shown in Fig. 3. A brief summary of the three rotors investigated in this work is provided in Table 1.

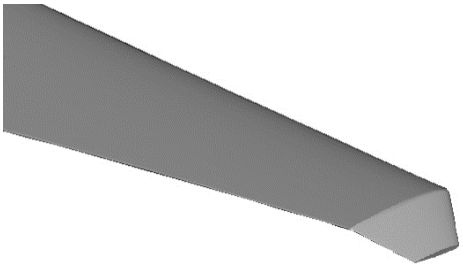

Figure 3: OPT5-MB blade visualization.

Mid-Fidelity Tools

A multifidelity computational strategy was used in this work, which consisted of two parts. The first part used CAMRAD II, which is a comprehensive rotorcraft analysis code allowing for the use of different wake models (e.g., uniform inflow, prescribed wake, and free-wake) and different blade dynamics (e.g., rigid and elastic). CAMRAD II requires aerodynamic airfoil coefficient data, which can either be generated using analytical equations or can be supplied by the user in the form of an airfoil table. CAMRAD II was used in this work for the OPT5 rotor with a general free-wake geometry model consisting of a single-peak vortex defined by the magnitude of maximum blade circulation, a second-order trapezoidal distortion integration, a second-order lifting-line with a quarter chord collocation point, and a wake extent of ten rotor revolutions. Since a symmetric NACA 0012 airfoil profile was used for the OPT5 blade design, a preexisting airfoil table in the C81 format was used throughout this work. The table was developed using experimental aerodynamic results over $-180° \leq \alpha \leq 180°$ and $0 \leq M_\infty \leq 1$ with a reference chord-based Reynolds number of $Re_c = 5.2x10^6$ at $M_\infty = 1$. The C81 table data were used by CAMRAD II for predicting spanwise aerodynamic forces and moments, which were then integrated over the entirety of the rotor to produce aerodynamic performance quantities, such as C_T and torque coefficient, C_Q. These mid-fidelity simulations were conducted in the hover operating condition at rotor speeds ranging from 2900 RPM $\leq \Omega \leq$ 5600 RPM (i.e., $0.27 \leq M_{\text{tip}} \leq 0.52$) to discern trends between predicted and experimental results reported in Ref. 1.

High-Fidelity Tools

The second part of the computational effort entailed the use of the lattice-Boltzmann method very-large-eddy simulation

Table 1: Characteristics of the three rotor cases.

Case	Airfoil geometry	Ω	Tip modification
OPT5	NACA 0012	5332 RPM	N/A
OPT5-MA (modified airfoil)	NACA 63A-612	4355 RPM	N/A
OPT5-MB (modified blade)	NACA 0012	5332 RPM	20° anhedral outboard of $0.95R$, 20° backward sweep outboard of $0.95R$, and additional taper ($c_{\text{tip}} = 0.485$ in) outboard of $0.95R$

(LBM-VLES) software, PowerFLOW, to simulate the OPT5 and OPT5-MB rotors at the design operating condition of $\Omega =$ 5332 RPM and the OPT5-MA rotor at $\Omega = 4355$ RPM. The reader is referred to Refs. 18, 19 for a detailed theoretical explanation of LBM. Since, in general, LBM involves the use of a Cartesian mesh with isotropic volumetric cells (i.e., voxels), the use of body-fitted, stretched boundary layer grids, like those commonly associated with Navier-Stokes solvers, is not possible. This places a stringent requirement on the number of near-body voxels required to resolve the boundary layer. To circumvent the computational cost associated with this high voxel count, PowerFLOW employs wall-functions in the first voxel adjacent to the geometry to model the boundary layer. An unreleased beta version of PowerFLOW, capable of resolving noise-generating boundary layer turbulence (Ref. 20) associated with transitional flow regimes, was used throughout this work with transitional wall-functions (Ref. 21) in the first cell adjacent to the rotor geometry.

The computational domain for each of the three LBM-VLES simulations was discretized in a similar fashion to what was done in Ref. 13, which is shown in Fig. 4 for the OPT5 rotor. The boundary of two adjacent variable resolution (VR) regions contains hanging nodes, where the voxels in the coarser region are twice as large as voxels in the adjacent, finer region, as shown in Fig. 4c. An outer cuboidal domain, extending $50R$ away from the center of the rotor in all directions, was used in this work with a cylindrical VR region dedicated to resolving rotor wake extending $2.25R$ away from the center of the rotor. Additionally, the finest voxel size in the VR region adjacent to the rotor was defined to be $\Delta s = c_{\text{tip}}/400$. The dimensional value of this finest voxel size and correspondent y^+ values at different spanwise locations have been tabulated in Table 2.

A VR region containing the rotor geometry and first three VR regions, shown in Fig. 4b, was also defined with a rotational speed equivalent to $\Omega = 5332$ RPM for the OPT5 and OPT5-MB rotor cases and $\Omega = 4355$ RPM for the OPT5-MA rotor case. Interpolation was used between this rotational VR region and the adjacent stationary computational domain. A no-slip boundary condition was imposed on the rotor and hub surfaces. STP conditions, as well as a zero velocity condition, were also imposed on the outer cuboidal boundaries of the computational domain. Each simulation was conducted over 16 rotor revolutions with the last seven being used for acoustic data analysis. The computational cost associated with each simulation was estimated to be approximately 1 million CPU hours.

Acoustic Post-Processing

Unsteady blade loading was sampled over the last seven predicted rotor revolutions at a rate of 133 kHz. These sampled data were then provided to PowerACOUSTICS 6-2021 for the computation of propagated acoustic pressure time history (APTH) at defined observer locations using an impermeable source-time-dominant implementation of Farassat's F1A (Refs. 22, 23). The seven revolutions of predicted APTH data were separated into seven equally sized partitions correspondent to each revolution of rotor data. These revolutions of data were averaged together to obtain a mean revolution of APTH, which is the periodic (i.e., tonal) noise signal. This tonal noise component was then subtracted from the raw, aperiodic APTH from the seven revolutions of predicted APTH data, and the resultant residual APTH served as the stochastic (i.e., broadband) noise signal. This technique for periodic averaging and broadband noise extraction has been applied extensively to both experimental and computational data with great success in previous work (Refs. 9, 13, 24).

The mean rotor revolution of predicted data was repeated enough times to attain a $\Delta f = 10$ Hz frequency resolution, which was then processed by treating the repeated rotor revolution data as an aperiodic signal, computing the fast Fourier transform (FFT) of the data, then using Eq. 3 to produce a narrowband spectrum of the predicted tonal noise sound pressure level (SPL);

$$\text{SPL} = 10\log_{10}\left(\frac{P_{xx} * \Delta f}{p_{ref}^2}\right), \tag{3}$$

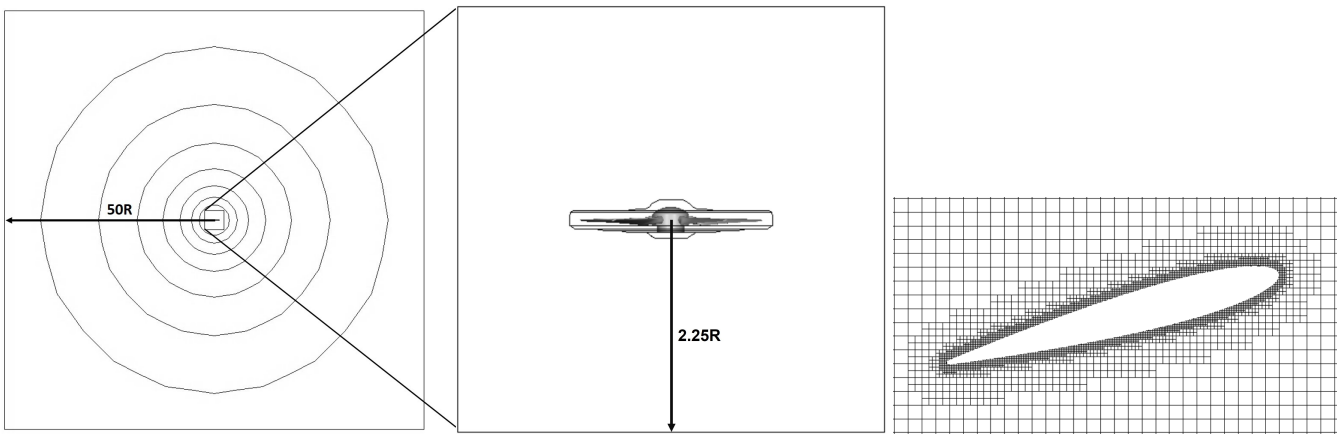

(a) Full computational domain. (b) Dedicated wake resolution region. (c) Near-field resolution along rotor blade.

Figure 4: High-fidelity computational domain visualization.

Table 2: Finest voxel size attributes.

Spanwise Location	c_r (in)	y^+	Voxel Size (in)	Voxel Size ($\%c_{\text{tip}}$)
$0.50R$	1.94	16.67		
$0.75R$	1.46	24.80	0.00243	0.25
R	0.97 (0.485 for OPT5-MB)	33.35 (35.04 for OPT5-MB)		

where P_{xx} is the resultant power spectral density from the FFT calculation and $p_{ref} = 20\ \mu$Pa.

The extracted broadband noise signal from the computations was treated as an aperiodic signal, over which an FFT was also calculated with a bin width of $\Delta f = 100$ Hz. The large bin width was required due to the limited revolutions of APTH data to reduce random uncertainty in the autospectrum. Equation 3 was used to produce a narrowband spectrum of the broadband noise, which was then used to generate one-third octave band ($SPL_{1/3}$) representations.

These tonal and broadband noise post-processing techniques were used on APTH data at both an in-plane and out-of-plane observer location. The in-plane observer location was located $y = 6.62$ ft (i.e., $y = 6.62R$) away from the rotor and was used to compare predicted results from the OPT5 rotor case to preliminary experimental measurements, which were processed in a similar manner. The out-of-plane observer was also located $y = 6.62$ ft away from the rotor but was $\Theta_{obs} = 45°$ below the rotor plane. Because broadband noise has a dipole directivity for hovering rotors, this out-of-plane observer location was deemed appropriate for comparing predicted results from the three rotor cases.

Since BWI noise generated by perpendicular BVI was thought to be a dominant broadband noise source, each blade from the three computational cases was split into various regions, similarly to what was done in Refs. 9, 10. This methodology allowed for the isolation of broadband noise emanating from the different blade regions and for the identification of different aerodynamically induced noise sources (i.e., BWI noise and separation noise). The split blade geometries for the OPT5 and OPT5-MB cases are shown in Fig. 5. It should be noted that the split blade geometry for the OPT5-MA was identical to that of the OPT5.

The inboard region, Region I, spanned from the hub to $r \leq 0.5R$ of the blade and included both the suction and pressure side blade surfaces. The second region, Region II, spanned from $0.5R < r \leq 0.75R$ and only included the suction and pressure side blade surfaces from $0.25c < x_c \leq c$. Region III encompassed the leading edge up to the quarter-chord location, $0 \leq x_c \leq 0.25c$, of both the suction and pressure sides of the blade between $0.5R < r \leq 0.75R$. Similarly, Regions IV and V spanned the outer $0.25R$ of the blade ($0.75R < r \leq R$) for the OPT5 and OPT5-MA cases and the outer $0.2R$ of the blade ($0.75R < r \leq 0.95R$) for the OPT5-MB case. Regions IV and V included the suction and pressure side surfaces from $0.25c < x_c \leq c$ and $0 \leq x_c \leq 0.25c$, respectively. Region VI included both the suction and pressure sides of the OPT5-MB blade over the modified portion of the blade span ($0.95R < r \leq R$). Regions VII and VIII, not shown in Fig. 5, correspond to the rotor hub and the end cap at the blade tip, respectively. A summary of the spanwise and chordwise extents of Regions I–VI is given in Table 3.

Table 3: Split rotor blade region summary (* indicates applicability to the OPT5-MB case only).

Region	Spanwise Extents	Chordwise Extents
I	$r \leq 0.5R$	$0 \leq x_c \leq c$
II	$0.5R < r \leq 0.75R$	$0.25c < x_c \leq c$
III	$0.5R < r \leq 0.75R$	$0 \leq x_c \leq 0.25c$
IV	$0.75R < r \leq R(0.95R^*)$	$0.25c < x_c \leq c$
V	$0.75R < r \leq R(0.95R^*)$	$0 \leq x_c \leq 0.25c$
VI*	$0.95R < r \leq R$	$0 \leq x_c \leq c$

The broadband noise post-processing techniques discussed previously were used over each region of the split rotor geometries shown in Fig. 5 at the out-of-plane observer location to compare the relative importance of noise emanating from the different regions of the rotor blade as well as to compare these broadband noise sources among the three rotor cases.

MID-FIDELITY RESULTS

Aerodynamic Results

CAMRAD II was used to predict C_T and C_Q of the OPT5 rotor case in the hover operating condition under variable rotor

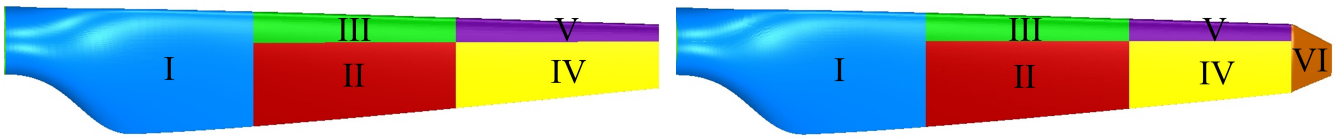

(a) OPT5 and OPT5-MA.

(b) OPT5-MB.

Figure 5: View of split rotor blade surface.

speeds, which are compared to experimental measurements in Fig. 6. It can be seen in Fig. 6b that the predicted C_Q agrees well with the measured results; however, C_T was overpredicted by no less than 43.19% relative to the experimental data for all simulated M_{tip} values, shown in Fig. 6a. It can also be seen that the predicted C_T trend deviates from the experimental results. Dimensionally, this corresponds to a thrust prediction of $T_{CII} = 58.39$ lb at the design condition of $\Omega = 5332$ RPM, which is similar to the target design thrust of $T_{\text{design}} = 62.85$ lb acquired using BEMT with the assumption of uniform inflow. This is in stark contrast to the experimentally measured thrust value of $T_{meas} = 38.66$ lb.

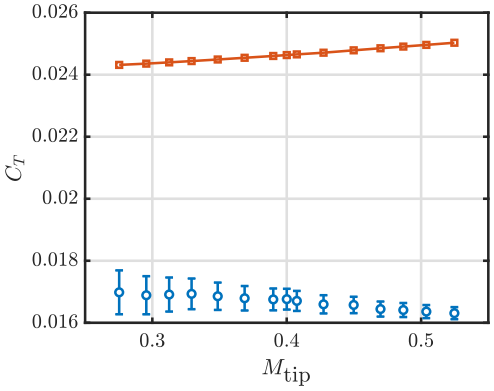

(a) Dimensionless thrust comparison.

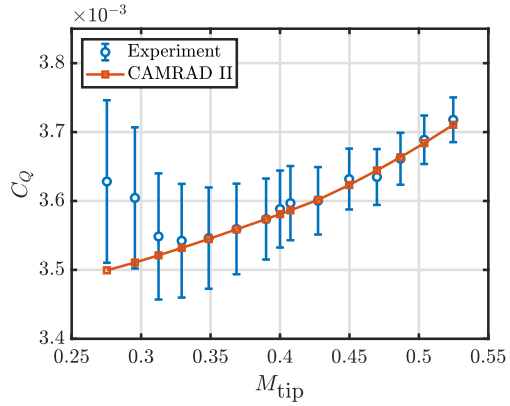

(b) Dimensionless torque comparison.

Figure 6: OPT5 aerodynamic performance characteristics.

As will be shown in the next section, the aerodynamic performance differences between measurements and mid-fidelity predictions are the result of outboard separation on the blade suction side induced by a perpendicular BVI as well as by inflow variation discrepancies in the mid-fidelity tools. To further verify that this perpendicular BVI was not captured by CAMRAD II, spanwise α values for the OPT5 at the design operating condition of $\Omega = 5332$ RPM are shown in Fig. 7.

Very little variation in α can be seen across the span of the OPT5 rotor in Fig. 7, except for inboard of $0.5R$. In the presence of perpendicular BVI, one would expect to see increased values of α outboard of the BVI and decreased α values inboard of the BVI, which was not captured by CAMRAD II. It

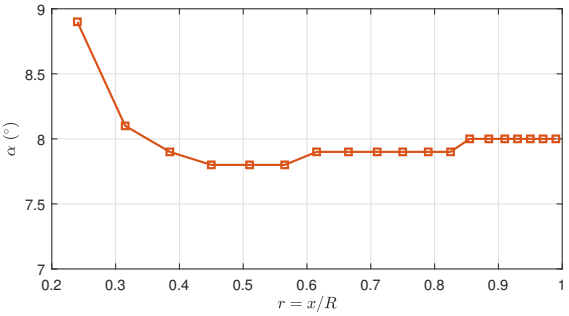

Figure 7: OPT5 angle of attack distribution at $\Omega = 5332$ RPM predicted by CAMRAD II.

is evident from Figs. 6 and 7 that the mid-fidelity method used in this work failed to adequately predict flow features responsible for the measured underperformance of the OPT5 rotor, elucidating the need for higher-fidelity predictions.

HIGH-FIDELITY RESULTS

Aerodynamic Results

PowerFLOW was used to simulate the OPT5 and OPT5-MB rotor cases at the design hover operating condition of $\Omega = 5332$ RPM and the OPT5-MA rotor case at $\Omega = 4355$ RPM. A summary of the dimensional aerodynamic performance results from both CAMRAD II and PowerFLOW is shown in Table 4. The thrust value predicted by PowerFLOW for the OPT5 rotor case agrees much better with the measured value of $T_{meas} = 38.66$ lb, with an overprediction of approximately 12%. Table 4 also shows that the thrust predicted using CAMRAD II for the OPT-MA rotor case at $\Omega = 4355$ RPM closely matched that of the OPT5 rotor, signifying that the OPT5-MA was properly thrust matched to the OPT5. The PowerFLOW results in Table 4 show that the OPT5, OPT5-MA, and OPT5-MB rotor cases all perform similarly in terms of predicted thrust and torque.

To identify the aerodynamic behavior responsible for the thrust differences between measured data and mid-fidelity predictions, oil flow visualization from the experiment (Ref. 1) was first compared to predicted velocity magnitude, V_{mag}, contours between 0 ft/s $\leq V_{mag} \leq$ 492.0 ft/s for the OPT5 rotor case, which is shown in Fig. 8. The exact details of the type of oil used and the duration of run time prior to ultraviolet light visualization can be found in Ref. 1. It can be seen that there is a region of flow separation on the suction side over the outboard portion of the blade span (i.e., approximately $0.88R$), which is captured both experimentally and computationally. Since, in general, most of the blade loading comes from the outboard portion of a rotor blade, it can be said that this flow separation is a likely culprit for the drastic underperformance of the OPT5 rotor when compared to the design condition.

Flow visualization of the vertical component of velocity (i.e., orthogonal to the rotor plane), V_z, and turbulent kinetic energy,

Table 4: Aerodynamic performance comparison at the design operating condition.

Case	Experiment	CAMRAD II		PowerFLOW		
	OPT5	OPT5	OPT5-MA	OPT5	OPT5-MA	OPT5-MB
Thrust	38.66 lb	58.39 lb	58.55 lb	43.32 lb	39.17 lb	42.93 lb
Relative Difference		51.03%		12.05%		
Torque	8.72 ft-lb	8.71 ft-lb	9.65 ft-lb	7.59 ft-lb	6.60 ft-lb	7.32 ft-lb
Relative Difference		0.11%		12.96%		

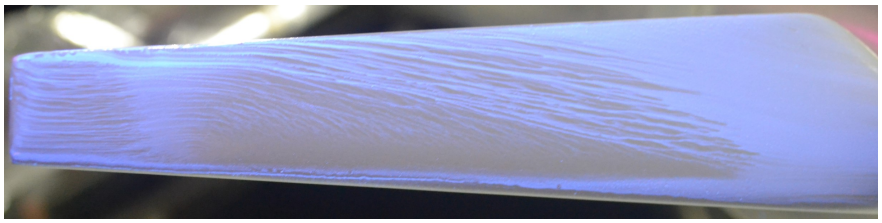

(a) Experimental oil flow visualization.

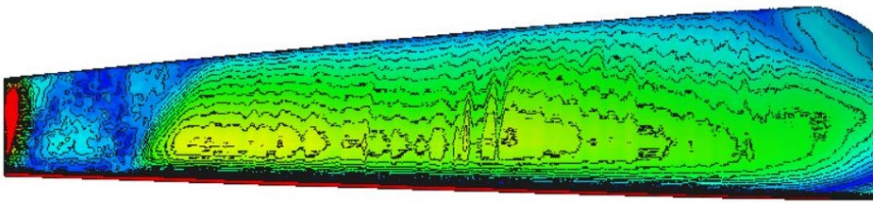

(b) PowerFLOW velocity magnitude on OPT5 blade surface (levels ranging from 0 ft/s $\leq V_{mag} \leq$ 492.0 ft/s).

Figure 8: OPT5 surface flow visualization.

TKE, were produced for the OPT5, OPT5-MA, and OPT5-MB rotor cases, which are shown in Figs. 9 and 10, respectively. These figures verify that the outboard flow separation of the OPT5 rotor case is indeed due to a perpendicular BVI. All rotor blades in Figs. 9 and 10 are contoured by V_z between -180.5 ft/s $\leq V_z \leq 65.5$ ft/s.

It can be seen from the TKE contours shown in Fig. 10a that the leading edge of the OPT5 rotor blade is in close proximity to the convected tip vortex of a preceding blade (i.e., small vortex miss distance) and that the blade is well within the vortex region of influence, or the turbulent field surrounding the vortex core. It can also be ascertained from Figs. 9a, 10a, and 8b that the center of the convected vortex core from the preceding blade is aligned with the onset of flow separation around approximately $0.88R$. Since the vortex shown in Figs. 9a and 10a is rotating clockwise in the displayed frame of reference, it is expected that the outboard-most point of the vortex would produce the highest positive vertical velocity and that the opposite would be true for the inboard-most point of the vortex, which is verified by the illustration of the vertical velocity component, or Fig. 9a. This figure also shows that the region of separation on the blade suction side has a strong upward velocity component, which is believed to be caused by the vortex-induced upwelling leading to forced separation. It can also be seen in Fig. 9a that inboard of the separation (i.e., $0.88R$), there is a strong downward velocity component, also believed to be caused by vortex-induced downwelling. It is thought that this downwelling would have a stabilizing effect on the boundary layer.

A few observations can be made by comparing V_z and TKE between the OPT5 and OPT5-MA rotor cases in Figs. 9 and 10. First, it can be seen that the tip vortex of a preceding blade is much stronger for the OPT5-MA rotor case when compared to that of the OPT5 rotor, though the preceding tip vortex of the OPT5-MA rotor does appear to have a slightly larger vortex miss distance, or distance between the vortex core and leading edge of a subsequent blade, than for the OPT5 rotor. It can also be seen by comparing surface values of V_z between the OPT5 and OPT5-MA cases in Figs. 9a and 9b that flow separation is not readily apparent on the suction side of the OPT5-MA blade. Since the OPT5-MA blades have a cambered airfoil profile, at the thrust matched condition of $\Omega = 4355$ RPM, the spanwise α values for OPT5-MA blade are lower than for the OPT and OPT5-MB cases. These lower α values, in addition to the better stall characteristics of the NACA 63A-612 of the OPT5-MA rotor when compared with the NACA 0012 of the OPT5, should mean that the OPT5-MA is less susceptible to separation caused by the perpendicular BVI, which appears to be the case in Fig. 9b.

In comparing the OPT5 to the OPT5-MB rotor cases, it can be seen in Figs. 9 and 10 that the preceding tip vortex for the OPT5-MB is both weaker than that of the OPT5 and exhibits a larger vortex separation distance. The decrease in vortex strength and increase in separation distance are thought to be

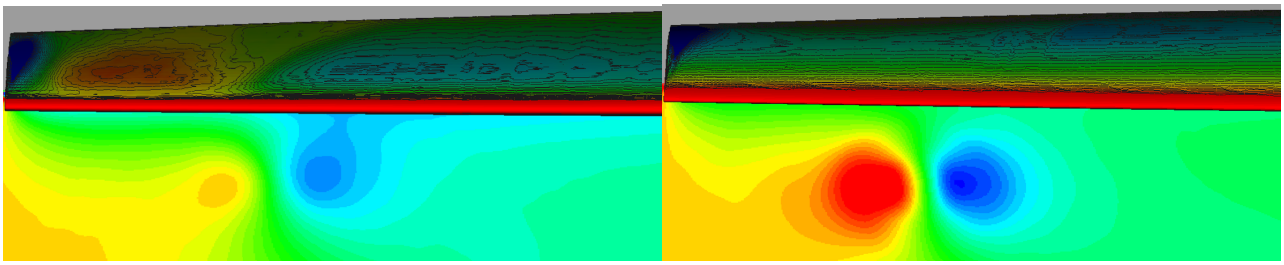

(a) OPT5. (b) OPT5-MA.

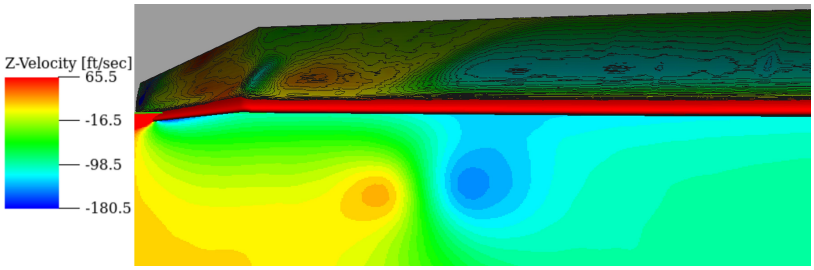

(c) OPT5-MB.

Figure 9: Flow visualization of V_z along a leading edge aligned vertical slice. Blade surfaces are contoured by V_z between -180.5 ft/s $\leq V_z \leq 65.5$ ft/s.

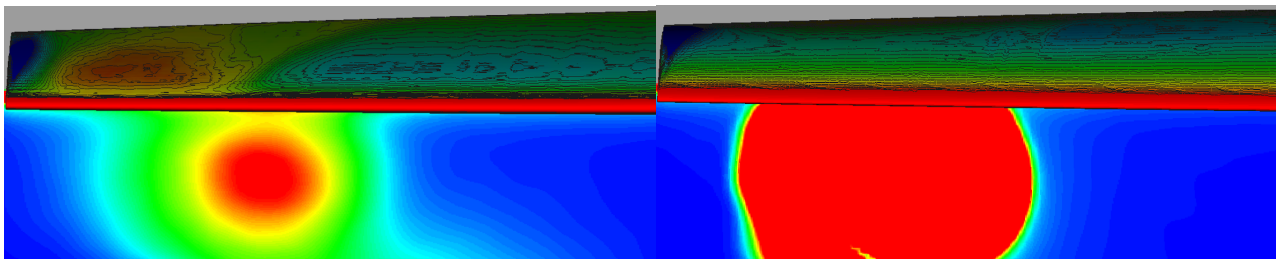

(a) OPT5. (b) OPT5-MA.

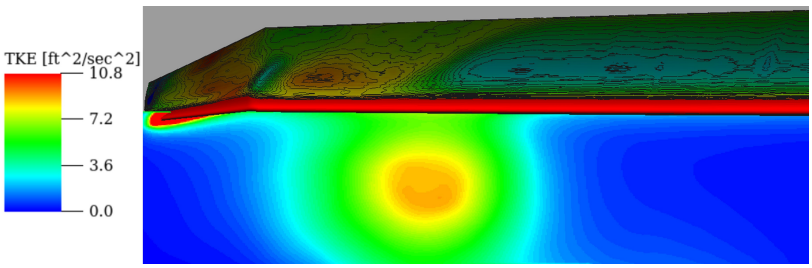

(c) OPT5-MB.

Figure 10: Flow visualization of TKE along a leading edge aligned vertical slice. Blade surfaces are contoured by V_z between -180.5 ft/s $\leq V_z \leq 65.5$ ft/s.

attributed to the additional outboard taper of the OPT5-MB blade and the anhedral/sweep, respectively. The spanwise extent of the vortex-induced separation on the OPT5-MB blade also appears to be similar to that of the OPT5 rotor case and can be seen to occur in Regions IV and VI. The similar operating conditions, airfoil geometry (i.e., NACA 0012), and outboard separation between the OPT5 and OPT5-MB rotors could explain the similar aerodynamic performance characteristics of these two cases shown in Table 4.

Though the illustrations in Figs. 9 and 10 provide qualitative insight toward a perpendicular BVI being the likely culprit for outboard flow separation and subsequent aerodynamic performance deficit of the OPT5 and OPT5-MB rotor cases, the similar low performance observed for the OPT5-MA rotor is still ambiguous since Figs. 9b and 10b show no indication of vortex-induced separation. To further investigate this, the pressure distribution at the $0.75R$ spanwise location predicted by PowerFLOW for the OPT5-MA rotor is compared to an XFOIL prediction for an NACA 63A-612 airfoil in Fig. 11, where the value of α was varied in XFOIL until the suction peak matched that of the PowerFLOW prediction. The XFOIL prediction was conducted using the Mach number and

Reynolds number corresponding to the $0.75R$ spanwise location (i.e., $M_\infty = 0.31$ and $Re_c = 263,696$).

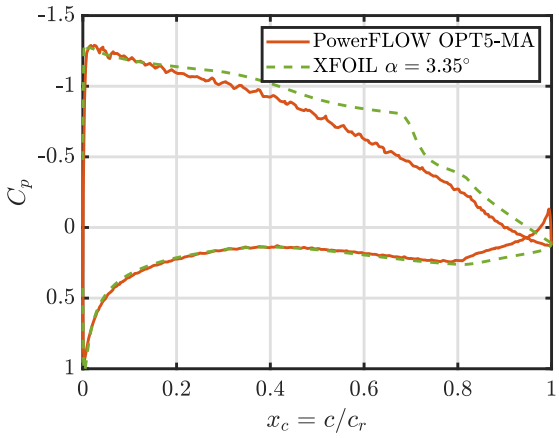

Figure 11: Comparison of the pressure distribution at $0.75R$ for the OPT5-MA rotor case.

It can be seen in Fig.11 that the heuristically determined value of $\alpha = 3.35°$ produced reasonable agreement between the extracted pressure distribution from PowerFLOW and the predicted distribution using XFOIL. It should be noted that the value of α at $0.75R$ predicted using CAMRAD II for the OPT5-MA case was approximately $\alpha = 5.9°$, elucidating that the inflow variation between PowerFLOW and CAMRAD II differs. To support this claim, the empirical inflow correction factor for hover in CAMRAD II, κ_h, was increased from the default value of $\kappa_h = 1.1$ to a value of $\kappa_h = 1.6$, such that the approximated value of $\alpha = 3.35°$ at $0.75R$ between the PowerFLOW prediction and CAMRAD II were matched. Using this new value of $\kappa_h = 1.6$ in CAMRAD II, the predicted thrust and torque of the OPT5-MA at $\Omega = 4355$ RPM were $T_{CII} = 42.79$ lb and $Q_{CII} = 8.79$ ft-lb, which agree better with the OPT5-MA PowerFLOW prediction shown in Table 4. This justification, along with the absence of vortex-induced separation for the OPT5-MA rotor, indicate that different inflow variation between CAMRAD II and PowerFLOW is the cause of the predicted aerodynamic performance difference for this rotor case. This difference in inflow variation also suggests that the OPT5-MA rotor was not thrust matched appropriately to the design condition and that a value of $\kappa_h = 1.6$ should be used with CAMRAD II to redetermine the value of Ω to generate the desired amount of thrust (i.e., $T_{\text{design}} = 62.85$ lb) for the OPT5-MA rotor. Furthermore, the vortex-induced separation of the OPT5 rotor may not account entirely for the aerodynamic performance difference between the measured data and design condition, with inflow variation differences likely being a secondary cause. It should be noted that though the OPT5-MA was not adequately thrust matched to the design condition, it was still thrust matched to the OPT5 operating condition, implying a one-to-one comparison of all subsequent acoustic results.

A similar approach was used with the OPT5 rotor shown in Fig. 12, where $\alpha = 5.8°$, determined using XFOIL for an NACA 0012 airfoil profile, produced good comparison to the extracted pressure distribution at $0.75R$ from the OPT5 PowerFLOW simulation. The empirical constant in CAMRAD II was changed from the default value of $\kappa_h = 1.1$ to a value of $\kappa_h = 1.55$ to match the α value at $0.75R$ predicted by CAMRAD II to the $\alpha = 5.8°$ estimate from the PowerFLOW simulation. The resulting thrust and torque predicted using CAMRAD II were $T_{CII} = 46.01$ lb and $Q_{CII} = 7.72$ ft-lb. This predicted thrust agrees much better with the experimentally measured value of $T_{meas} = 38.66$ lb, and the results from the CAMRAD II prediction using $\kappa_h = 1.55$ signify that the vortex-induced separation (not captured by CAMRAD II) might only be responsible for 20% of the 51.03% difference for the OPT5 in Table 4, with the other 31.03% being caused by inflow variation differences. This implies that mid-fidelity tools may not be well-suited for the preliminary design of small unconventional rotors, like those associated with AAM, in hover operating conditions, without prior experimental or computational knowledge of the inflow or spanwise loading conditions. Even with prior aerodynamic knowledge, mid-fidelity tools may not adequately predict vortex-induced separation.

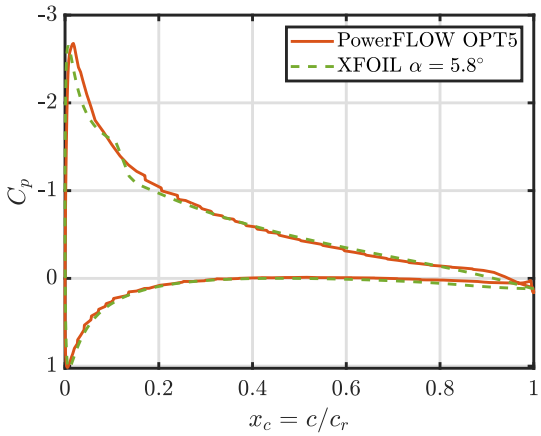

Figure 12: Comparison of the pressure distribution at $0.75R$ for the OPT5 rotor case.

Aeroacoustic Results

Preliminary measurements for both the tonal and broadband noise at the in-plane observer location ($\Theta_{obs} = 0°$ and $y = 6.62$ ft) were compared to predictions conducted using PowerFLOW for the OPT5 rotor and are shown in Fig. 13. It can be seen in Fig. 13 that both the tonal noise at the fundamental and second harmonic of the blade passage frequency (BPF) and broadband noise are underpredicted from the experiment by approximately 10 dB. It should be noted that there was no acoustic treatment in the experimental facility. Phased array results suggest possible measurement contamination due to acoustic reflections. These reflections could attribute to the similar tonal and broadband noise underprediction. Further-

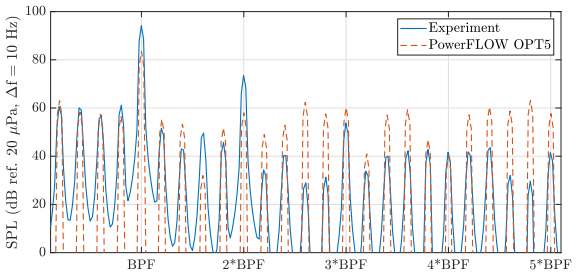

(a) Tonal noise narrowband spectra.

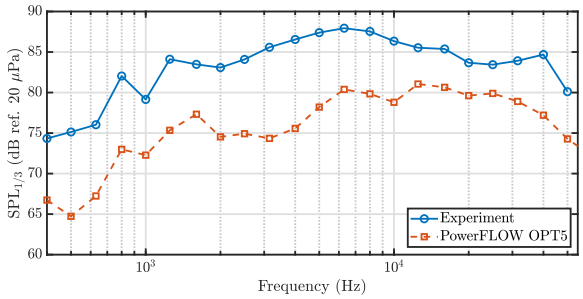

(b) Broadband noise one-third octave spectra.

Figure 13: Acoustic comparison between measured data and PowerFLOW predictions at the in-plane observer location ($\Theta_{obs} = 0^\circ$ and $y = 6.62$ ft).

more, broadband noise has a dipole directivity for isolated hovering rotors with an acoustic null region located in the rotor plane, meaning that in-plane observer locations may not be suitable for comparison. Though the experimental measurements are very preliminary, the comparison in Fig. 13 indicates reasonable agreement in the observed acoustic trends between measurements and predicted results.

Tonal and broadband noise comparisons among PowerFLOW predictions for the OPT5, OPT5-MA, and OPT5-MB rotor cases at the out-of-plane observer location are shown in Fig. 14. It should be noted that the tonal noise frequency for the OPT5-MA case shown in Fig. 14a was scaled to match that of the OPT5 and OPT5-MB cases for better comparison. Fig. 14a shows negligible difference between the OPT5 and OPT5-MB cases except at the second BPF harmonic, where the OPT5-MB case is approximately 13.5 dB quieter than the OPT5. The OPT5-MA rotor also appears to be quieter than the OPT5 at all BPF harmonics shown in Fig. 14. In comparing the broadband noise results in Fig. 14b, it can first be seen that broadband noise levels are higher than the tonal noise generated from each rotor case above approximately 1 kHz. It can also be seen that the OPT5-MB case generates approximately 4 dB less broadband noise than the OPT5 case across most frequencies shown in Fig. 14b. The effect of the vortex-induced separation is similar between the OPT5 and OPT5-MB cases; however, the preceding vortex for the OPT5-MB case is weaker than for the OPT5 case, as shown in Fig. 10. It is thought that this weaker preceding vortex caused by the outboard anhedral, sweep, and taper of the OPT5-MB is likely responsible for the decrease in broadband noise when compared to the OPT5 case. The OPT5-MA case, on the other hand, was shown to have a stronger preceding vortex than the OPT5 case in Fig. 10 but with no vortex-induced separation. Since the broadband noise levels for the OPT5-MA case are significantly lower than for the other two rotor cases, it can be said that the vortex-induced separation might be a dominant broadband noise source.

To further investigate the different broadband noise sources, results predicted for each of the split blade regions for the OPT5, OPT5-MA, and OPT5-MB rotors are shown in Fig. 15. It is again noted that Region VI, corresponding to the outboard blade modification for the OPT5-MB case, is not applicable to the OPT5 and OPT5-MA cases. Also, Region VII, correspondent to the hub, is not shown due to negligible acoustic significance and Region VIII corresponds to the end cap of the blade tip.

It can be seen in Fig. 15 that Region IV produces most of the broadband noise for all three rotor cases followed by Region V for the OPT5 and OPT5-MB cases. For the OPT5 and OPT5-MB cases, this signifies that the vortex-induced separation is the most dominant broadband noise generating mechanism, and for the OPT5-MA case, other broadband self-

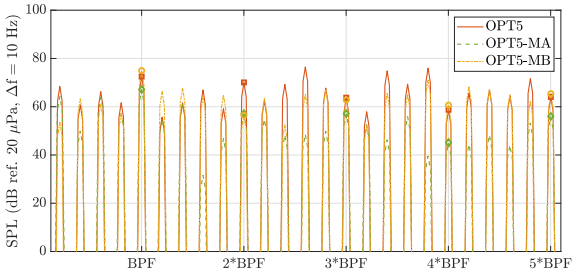

(a) Tonal noise narrowband spectra.

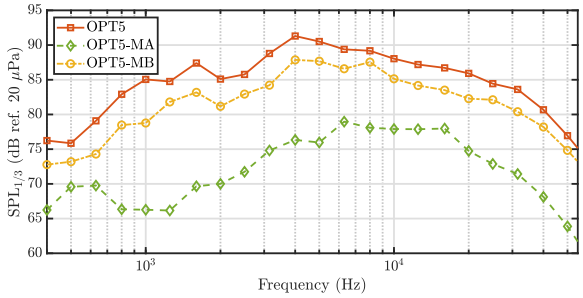

(b) Broadband noise one-third octave spectra.

Figure 14: Acoustic comparison among PowerFLOW predictions at the out-of-plane observer location ($\Theta_{obs} = 45^\circ$ and $y = 6.62$ ft).

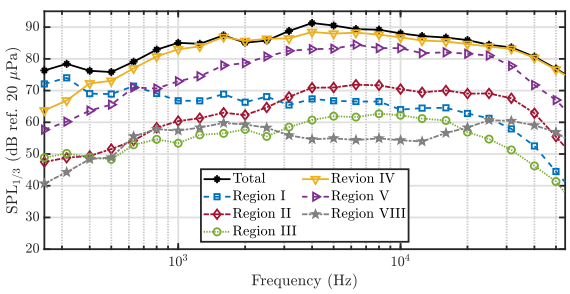

(a) OPT5.

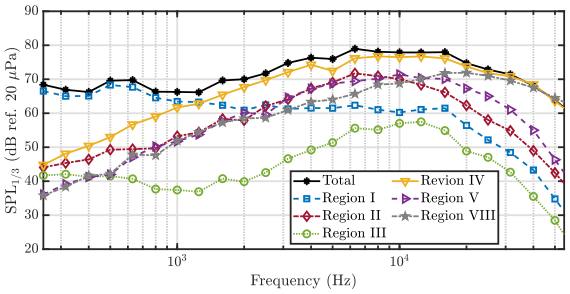

(b) OPT5-MA.

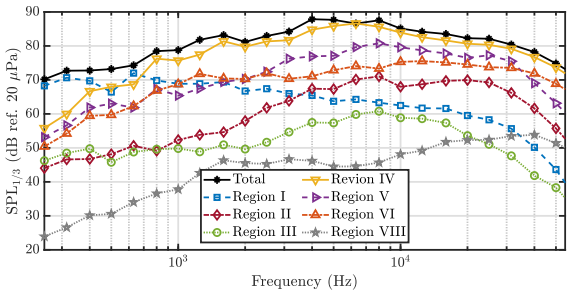

(c) OPT5-MB.

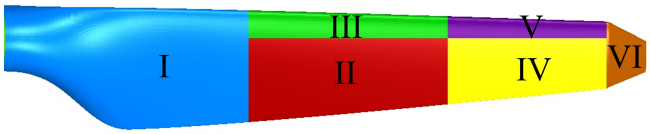

(d) Visualization of OPT5-MB split regions.

Figure 15: Broadband one-third octave spectra of split blade regions at the out-of-plane observer location ($\Theta_{obs} = 45^\circ$ and $y = 6.62$ ft).

noise mechanisms caused by boundary layer turbulence convection past the blade trailing edge are dominant. Since the perpendicular BVI occurs within Region V, the broadband noise from this region represents the resultant broadband BWI noise, which is the second-most dominant broadband noise source for the OPT5 case above 800 Hz and for the OPT5-MB case above 2500 Hz. Below 800 Hz for the OPT5 and 2500 Hz for the OPT5-MB cases, broadband noise from the inboard region, Region I, is seen to be second-most dominant. It can also be seen for the OPT5-MB case in Fig. 15c that the modified blade tip outboard of $0.95R$ (i.e., Region VI) generates substantial broadband noise, likely due to the vortex-induced separation, which was shown to occur in both Regions IV and Region VI for the OPT5-MB case.

As discussed previously, the OPT5-MA case did not show signs of vortex-induced separation meaning that the flow physics and subsequent aeroacoustics behave closer to what one may expect. Though the preceding vortex is stronger for the OPT5-MA case, the BWI noise is lower than that of the other two rotor cases. This result agrees with the BWI noise dependency on C_T observed in Ref. 10, where the BWI noise decreased with increasing C_T (e.g., caused by increasing camber or collective pitch). Below 1250 Hz, Fig. 15b shows that the broadband noise from Region I is the dominant broadband noise source for the OPT5-MA rotor case. Also shown in this figure, the end cap at the blade tip (i.e., Region VIII) is seen to have comparable broadband noise levels to Region IV above 20 kHz. Region VIII represents the broadband self-noise caused by tip-vortex formation, and since it was shown previously that the OPT5-MA has a stronger tip vortex than the OPT5 and OPT5-MB cases, it is intuitive that tip-vortex formation noise is stronger for the OPT5-MA case when compared to the other two rotor cases.

CONCLUSIONS

This work computationally investigated the vortex-induced outboard separation from an optimum hovering 5-bladed rotor geometry (OPT5) observed in the NASA Langley Research Center 14- by 22-Foot Subsonic Tunnel. Experimental measurements showed that the thrust generated by this rotor was approximately 38.5% under the design thrust calculated using BEMT. In an effort to mitigate the vortex-induced outboard separation, two separate alterations were made to the OPT5 rotor geometry. The first of which, the modified airfoil (OPT5-MA) rotor case, modified the NACA 0012 airfoil profile to an NACA 63A-612 and the second, the modified blade (OPT5-MB) rotor case, added anhedral/sweep and additional taper to the outboard 5% of the blade, while still maintaining an NACA 0012 airfoil profile.

First, mid-fidelity predictions were performed for the OPT5 case using the free-wake solver in CAMRAD II, which showed an overprediction of the measured thrust by no less than 43.19% across a range of different rotor speeds. CAMRAD II was also used to determine a suitable rotor speed for the OPT5-MA such that it performed similarly to the OPT5 rotor in terms of dimensional thrust. CAMRAD II also showed no evidence of vortex-induced separation. Then, high-fidelity predictions were performed using the lattice-Boltzmann solver, PowerFLOW, for the OPT5, OPT5-MA, and OPT5-MB rotor cases. These high fidelity predictions showed similar thrust generation among all three rotor cases

and more reasonable agreement between the OPT5 prediction and measured results. Comparison between the predicted velocity magnitude on the OPT5 blade surface to oil flow visualizations from the experiment showed that the vortex-induced separation predicted by PowerFLOW closely matched that of the experiment. The PowerFLOW simulation also showed that the OPT5-MA and OPT5-MB rotors had stronger and weaker tip vortices than the OPT5 rotor, respectively, with both the OPT5-MA and OPT5-MB having slightly larger vortex separation distances than the OPT5. The OPT5-MA prediction also showed no signs of vortex-induced separation, likely due to the increased stall angle from the NACA 63A-612 airfoil profile. Pressure distributions for the OPT5 and OPT5-MA cases at the $0.75R$ spanwise location were extracted from the PowerFLOW predictions and angle of attack values were heuristically determined using XFOIL by matching suction pressure peaks between XFOIL and the PowerFLOW predictions. These heuristically determined angles of attack were lower than those calculated using CAMRAD II, signifying inflow discrepancies with the BEMT-based mid-fidelity tools. The empirical inflow coefficient in CAMRAD II was increased until the angle of attack at the $0.75R$ spanwise location predicted by CAMRAD II matched the heuristically determined angle of attack from the PowerFLOW simulations for the OPT5 and OPT5-MA cases. The new CAMRAD II predictions using the increased empirical inflow coefficient for the OPT5 and OPT5-MA cases agreed better with the high-fidelity predictions for both cases and the measured data for the OPT5 case in terms of thrust generation. Since CAMRAD II was unable to predict vortex-induced separation, the new thrust prediction for the OPT5 rotor was used to determined that approximately 20% of the thrust discrepancy between the measurement and the original CAMRAD II prediction was caused by the vortex-induced separation, with another 31.03% being due to inflow discrepancies with the BEMT-based solvers used in this work.

Acoustic predictions performed using PowerACOUSTICS at an in-plane observer location were compared to measurements taken in the NASA Langley Research Center 14- by 22-Foot Subsonic Tunnel for the OPT5 rotor. The measured data were very preliminary in that the facility was not outfitted with acoustic treatment and may have been prone to acoustic reflections. Both the predicted tonal and broadband noise were underpredicted from the preliminary measurements by approximately 10 dB; however, they trended with the measurements reasonably well. Predictions for the OPT5, OPT5-MA, and OPT5-MB cases were compared and showed that the OPT5-MA was quieter than the OPT5 at all reported BPF harmonics and that there was negligible difference between the OPT5-MB and the OPT5, except at the second BPF harmonic, where the OPT5-MB was approximately 13.5 dB quieter than the OPT5. The broadband noise from the OPT5-MB case was approximately 4 dB less than the OPT5 across all reported frequencies. Since both the OPT5 and OPT5-MB showed vortex-induced separation, this broadband noise reduction observed with the OPT5-MB case was believed to be due to the vortex strength reduction caused by the anhedral/sweep and additional taper of the OPT5-MB. The broadband noise from the OPT5-MA rotor was exceptionally less than that of both the OPT5 and OPT5-MB cases due to the absence of vortex-induced separation resulting from the higher stall angle of the NACA 63A-612 airfoil on the OPT5-MA.

Lastly, the blades for the OPT5, OPT5-MA, and OPT5-MB rotors were split into various regions and broadband noise was calculated separately for each region to identify different noise generating mechanisms. It was shown that most of the broadband noise for all three cases emanated from the aft outboard blade region, primarily caused by vortex-induced separation for the OPT5 and OPT5-MB cases and other broadband self-noise sources for the OPT5-MA case. Broadband BWI noise caused by the perpendicular blade-vortex interaction was the second-most dominant noise source above 800 Hz for the OPT5 case and above 2500 Hz for the OPT5-MB case. Although the tip vortex was stronger for the OPT5-MA case compared with the OPT5 and OPT5-MB cases, the broadband BWI noise was shown to be lower for the OPT5-MA case. The tip vortex formation noise for the OPT5-MA case, however, was shown to be a dominant noise source above 20 kHz.

ACKNOWLEDGMENTS

The authors would like to thank Brandon Litherland from the Aeronautics Systems Analysis Branch at the NASA Langley Research Center for his work in designing the OPT5-MA rotor blades, Mehti Koklu from the Flow Physics and Control Branch at the NASA Langley Research Center for performing the oil flow visualization, and Doug Boyd from the Aeroacoustics Branch at the NASA Langley Research Center for his valuable CAMRAD II expertise and for fruitful discussions, which were vital to this work. This work was funded by the NASA Revolutionary Vertical Lift Technology (RVLT) project. Computational resources supporting this work were provided by the NASA High-End Computing (HEC) Program through the NASA Advanced Supercomputing (NAS) Division at the NASA Ames Research Center.

REFERENCES

1. Zawodny, N. S., Pascioni, K. A., and Thurman, C. S., "An Overview of the Proprotor Performance Test in the 14- by 22-Foot Subsonic Wind Tunnel," VFS International 79th Annual Forum & Technology Display, West Palm Beach, FL, May 2023.

2. Wittmer, K. S., Devenport, W. J., Rife, M. C., and Glegg, S. A. L., "Perpendicular Blade Vortex Interaction," *AIAA Journal*, Vol. 33, (9), 1995, pp. 1667–1674. DOI: 10.2514/3.12802

3. Wittmer, K. S., and Devenport, W. J., "Effects of Perpendicular Blade-Vortex Interaction, Part 1: Turbulence Structure and Development," *AIAA Journal*, Vol. 37, (7), 1999, pp. 805–812. DOI: 10.2514/2.7527

4. Wittmer, K. S., Devenport, W. J., and Glegg, S. A. L., "Effects of Perpendicular Blade-Vortex Interaction, Part 2: Parameter Study," *AIAA Journal*, Vol. 37, (7), 1999, pp. 813–817. DOI: 10.2514/2.7528

5. Brooks, T. F., Marcolini, M. A., and Pope, D. S., "Main Rotor Broadband Noise Study in the DNW," *Journal of the American Helicopter Society*, Vol. 34, (2), 1989, pp. 3–12. DOI: 10.4050/JAHS.34.2.3

6. Glegg, S. A. L., "Prediction of Blade Wake Interaction Noise Based on a Turbulent Vortex Model," *AIAA Journal*, Vol. 29, (10), 1991, pp. 1545–1551. DOI: 10.2514/3.10774

7. Glegg, S. A. L., Devenport, W. J., Wittmer, K. S., and Pope, D. S., "Broadband Helicopter Noise Generated by Blade Wake Interactions," *Journal of the American Helicopter Society*, Vol. 44, (4), 1999, pp. 293–301. DOI: 10.4050/JAHS.44.293

8. Brooks, T. F., and Burley, C. L., "Blade Wake Interaction Noise for a Main Rotor," *Journal of the American Helicopter Society*, Vol. 49, (1), 2004, pp. 11–27. DOI: 10.4050/JAHS.49.11

9. Thurman, C. S., Zawodny, N. S., Pettingill, N. A., Lopes, L. V., and Baeder, J. D., "Physics-informed Broadband Noise Source Identification and Prediction of an Ideally Twisted Rotor," AIAA SciTech 2021 Forum, Virtual, January 2021. DOI: 10.2514/6.2021-1925

10. Thurman, C. S., *Surrogate Modeling and Characterization of Blade-Wake Interaction Noise for Hovering sUAS Rotors using Artificial Neural Networks*, Ph.D. thesis, University of Maryland, College Park, MD, July 2022.

11. Ham, N. D., "Some Conclusions from an Investigation of Blade-Vortex Interaction," *Journal of the American Helicopter Society*, Vol. 20, (4), 1975, pp. 26–31. DOI: 10.4050/JAHS.20.26

12. Leishman, J. G., *Principles of Helicopter Aerodynamics*, Cambridge University Press, New York, NY, 2000.

13. Thurman, C. S., Zawodny, N. S., and Pettingill, N. A., "The Effect of Boundary Layer Character on Stochastic Rotor Blade Vortex Shedding Noise," VFS International 78th Annual Forum & Technology Display, Fort Worth, TX, May 2022. DOI: 10.4050/F-0078-2022-17428

14. Pettingill, N. A., Zawodny, N. S., and Thurman, C. S., "Aeroacoustic Testing of UAS-Scale Rotors for a Quadcopter in Hover and Forward Flight," 28th AIAA/CEAS Aeroacoustics 2022 Conference, Southampton, England, June 2022. DOI: 10.2514/6.2022-3110

15. Zawodny, N. S., Pettingill, N. A., and Thurman, C. S., "Identification and Reduction of Interactional Noise of a Quadcopter in Hover and Forward Flight Conditions," Internoise 2022, Glasgow, Scotland, August 2022.

16. Whiteside, S. K. S., Pollard, B. P., Antcliff, K. R., Zawodny, N. S., Fei, X., Silva, C., and Medina, G. L., "Design of a Tiltwing Concept Vehicle for Urban Air Mobility," NASA TM 2021-0017971, 2021.

17. Johnson, W., *CAMRAD II: Comprehensive Analytical Model of Rotorcraft Aerodynamics and Dynamics, Vols. I – VII*, Johnson Aeronautics, 2020.

18. Succi, S., *The Lattice Boltzmann Equation for Fluid Dynamics and Beyond*, Clarendon Press, Oxford, first edition, 2001.

19. Shan, X., Yuan, X.-F., and Chen, H., "Kinetic Theory Representation of Hydrodynamics: A Way Beyond the Navier-Stokes Equation," *Journal of Fluid Mechanics*, Vol. 550, 2006, pp. 413–441. DOI: 10.1017/S0022112005008153

20. Casalino, D., Romani, G., Zhang, R., and Chen, H., "Lattice-Boltzmann Calculations of Rotor Aeroacoustics in Transitional Boundary Layer Regime," *Aerospace Science and Technology*, Vol. 130, (107953), 2022. DOI: 10.1016/j.ast.2022.107953

21. Duda, B., Fares, E., Kotapati, R., Li, Y., Staroselsky, I., Zhang, R., and Chen, H., "Capturing Laminar to Turbulent Transition within the LBM based CFD solver PowerFLOW," AIAA Scitech 2019 Forum, 2019. DOI: 10.2514/6.2019-1832

22. Brentner, K., and Farassat, F., "Modeling aerodynamically generated sound of helicopter rotors," *Progress in Aerospace Sciences*, Vol. 39, (2–3), 2003, pp. 83–120. DOI: 10.1016/S0376-0421(02)00068-4

23. Farassat, F., "Derivation of Formulations 1 and 1A of Farassat," NASA TM 2007-214853, 2007.

24. Pettingill, N. A., Zawodny, N. S., Thurman, C. S., and Lopes, L. V., "Acoustic and Performance Characteristics of an Ideally Twisted Rotor in Hover," AIAA SciTech 2021 Forum, Virtual, January 2021. DOI: 10.2514/6.2021-1928